DOI: 10.1002/((please add manuscript number))
**Article type: Full paper**

# Comparison of the morphology development of polymer-fullerene and polymer-polymer solar cells during solution-shearing blade coating

*Xiaodan Gu, Hongping Yan, Tadanori Kurosawa, Bob C. Schroeder, Kevin L. Gu, Yan Zhou, John W. F. To, Stefan D. Oosterhout, Victoria Savikhin, Francisco Molina-Lopez, Christopher J. Tassone, Stefan C.B. Mannsfeld, Cheng Wang, Michael F. Toney*, Zhenan Bao**

Dr. X. Gu, Dr. T. Kurosawa, K. L. Gu, Dr. Y. Zhou, J. To, Dr. F. Molina-Lopez, Prof. Z. Bao
Department of Chemical Engineering, Stanford University, Stanford, CA 94305, United States
E-mail: zbao@stanford.edu

Dr. X. Gu, Dr. H. Yan, Dr. S. D. Oosterhout, V. Savikhin, Dr. C. J. Tassone, Dr. M. F. Toney
Stanford Synchrotron Radiation Light source, SLAC National Accelerator Laboratory, Menlo Park, California 94025, United States
E-mail: mftoney@slac.stanford.edu

Prof. S. C. B. Mannsfeld
Center for Advancing Electronics Dresden, Dresden University of Technology, 01062 Dresden, Germany

Dr. C. Wang
Advanced Light Source, Lawrence Berkeley National Laboratory, Berkeley, California 94720, United States

Dr. B. C. Schroeder
School of Biological and Chemical Sciences and Materials Research Institute, Queen Mary University of London, Mile End Road, London E1 4NS

Keywords: P3HT, PCBM, PNDIT, solution processing, real time X-ray scattering

Polymer solar cells hold the promise to be a low cost, mechanically robust renewable power source, possibly used in building integrated photovoltaics. During the past decades, considerable progress has been made in improving the performance of polymer solar cells, with single-junction power conversion efficiencies (PCEs) of over 11%, through optimizing active layer absorption, energy level matching and morphology. [1,2] However the acceptor molecules used in the bulk heterojunction (BHJ) of these solar cells are mostly limited to fullerene-based electron acceptors. There is a growing interest to replace fullerene acceptors with polymer acceptors to gain benefits including lower cost, broader light spectrum coverage

as well as improved mechanical and thermal stability[1,3,4]. More recently, non-fullerence polymer solar cells were reported to have the unique advantage of simultaneously minimizing voltage loss and keeping efficient charge generation and separation[5]. Among the various n-type semiconducting polymer structures investigated as electron acceptors in all-polymer solar cells to date, perylene diimide (PDI)[6-9] and naphthalene diimide (NDI)[10-17] based polymers have emerged as the most promising materials due to their high electron mobility. However, the performance of all-polymer solar cells composed of low band gap donor polymers and NDI or PDI based n-type semiconducting polymers has so far remained lower in PCE than the corresponding polymer:fullerene devices. For example, early work on blends of poly(3-hexylthiophene-2,5-diyl) (P3HT) and poly{[*N*,*N*' -bis(2-octyldodecyl)-naphthalene-1,4,5,8-bis(dicarbox- imide)-2,6-diyl]-alt-5,50-(2,2'2'-bithiophene)} [P(NDI2OD-T2); Polyera Activ Ink™ N2200] showed discouraging results with a PCE below 0.2%[18]. Poly({4,8-bis[(2-ethylhexyl)oxy]benzo[1,2-*b*:4,5-b′]dithiophene-2,6-diyl}{3-fluoro-2-[(2-ethylhexyl)carbonyl]thieno[3,4-*b*]thiophenediyl}) (PTB7), a high performance donor material with ~9% PCE when processed with PCBM acceptor[19], initially only showed 2.7% PCE, when blended with P(NDI2OD-T2) acceptor [19,20]. It has been suggested that unfavorable morphologies formed in the all-polymer cases by scanning near-field optical microscopy[21]. An early morphology study by X-ray scattering also indicated that large phase separation were formed for P3HT:Poly(9,9-dioctylfluorene-*alt*-benzothiadiazole) (F8BT) BHJ and P3HT:P(NDI2OD-T2) BHJ[22]. Additionally, spectroscopic results of all-polymer solar cells showed that charge separation was adversely affected by geminate recombination in sub-nanosecond time scales due to unfavorable morphology [21-25]. Only very recently has the performance of all-polymer solar cells begun to approach that of polymer-fullerene blends, with the use of the poly[4,8-bis(5-(2-ethylhexyl)thiophen-2-yl)benzo[1,2-b;4,5-b']dithiophene-2,6-diyl-alt-(4-(2-ethylhexyl)-3-fluorothieno[3,4-b]thiophene-)-2-carboxylate-2-6-diyl)] (PTB7-Th) or benzodithiophene-alt-benzo- triazole copolymers as the donor

polymer and N2200 as acceptor polymer. [11,26,27] More recently, a combination of a conjugated polymer (PBDB-T: poly[(2,6-(4,8-bis(5-(2-ethylhexyl)thiophen-2-yl)- benzo[1,2-b:4,5-b']dithiophene))-alt-(5,5-(1',3'-di-2-thienyl-5',7'- bis(2-ethylhexyl)benzo[1',2'-c:4',5'-c']dithiophene-4,8-dione))]) and small molecular compound (ITIC: 3,9-bis(2-methylene- (3-(1,1-dicyanomethylene)-indanone))-5,5,11,11-tetrakis(4- hexylphenyl)-dithieno[2,3-d:2',3'-d']-s-indaceno[1,2-b:5,6-b'] dithiophene) were used to make BHJ solar cells with a high PCE of 11%[2].

Developing high performance all-polymer BHJ devices requires an understanding of the morphology differences originating from the fullerene and polymer acceptors. A range of methods are well-established to investigate the morphology of polymer:fullerene solar cells, including real-space imaging methods and X-ray scattering and neutron scattering[28-31], as well as secondary ion mass spectrometry (SIMS) and X-ray photoelectron spectroscopy (XPS) for vertical chemical composition distribution[32]. However, these characterizations are performed on completed thin films, not during the film forming drying process. Thus, previous works lack of information about the morphology development process and elucidating these film formation processes may be a key to understanding and controlling the morphology, which gives the drastic performance differences among different cell types.

Real-time X-ray diffraction can monitor the morphology evolution of the BHJ during the drying process[33,34]. It has been used to understand the morphology development for polymer:fullerene cell as well as small molecule:fullerene cells[33,35-43]. For example, Amassian *et al.* used real time X-ray scattering to directly probe the formation of the photoactive layer by spin-coating[43]. They observed co-occurrence of crystallization and phase separation in P3HT:PCBM blends during solvent evaporation. Barrena *et al.* examined the structure evolution of doctor blade coated P3HT:PCBM solar cells to understand

morphology evolution for the P3HT donor [40-42]. Similarly, Herzig *et al.* examined the structure evolution of slot-die coated P3HT:PCBM solar cells[34], and Russll *et al.* examined the examined the structure evolution of slot-die coated diketopyrrolopyrrole and quaterthiophene (DPPBT) :PCBM solar cells[38]. More recently, Richter and DeLongchamp *et al.* used real-time X-ray diffraction to understand the solvent additive effect in polymer:fullerene and small-molecules:fullerene solar cells.[36,37] It has been shown that real-time X-ray diffraction is a powerful tool to track down the polymer crystallization during the drying process.

Here, we combine in situ, real-time wide angle X-ray scattering and optical interferometry with *ex situ* hard and soft X-ray scattering to understand the morphology evolution of all-polymer solar cells and contrast this with polymer:fullerene cells. This work sheds light on the challenges, such as large favorable phase separation, faced by all-polymer solar cells. To the best of our knowledge, this is the first report for real-time time characterization of all-polymer solar cells BHJ during solution processing. We found that the high glass transition temperature of fullerene and the tendency of the polymer to intermix with fullerene is critical in preventing the donor polymer from forming large domains. Meanwhile, the polymer acceptor showed a glass transition temperature lower than room temperature, allowing both donor and acceptor polymers to crystallize in the late stage of drying with a resulting large-scale phase separation, which has negative impact on charge extraction, since large domains result in exciton recombining before they reach the donor:acceptor interface.

In order to understand the influence of the different acceptors on the thin film morphology, two model systems were investigated: P3HT:[6,6]-Phenyl-C61-butyric acid methyl ester ($PC_{61}BM$), and P3HT:naphthalene diimide thiophene-based (PNDIT) acceptor (**Figure 1a**). For the *in situ* study of the structural evolution during the printing process, a solution of

P3HT:PCBM 1:1 blends or P3HT:PNDIT 1:1 blends dissolved in chlorobenzene (CB) was solution-sheared on silicon substrates at 35 °C[44-46]. During the printing, the gap between the hydrophobic treated silicon blade and silicon substrate was fixed at 250 µm. A printing speed of 6 cm/s was used to obtain a relatively thick film in order to improve the signal to noise ratio for the diffracted X-ray. The intensity of X-ray was attenuated by a factor of 30 to reduce beam damage to the sample. We observed strong beam damages to the samples in halogenated solvents with the use of X-ray beam without attenuation. The real-time X-ray scattering data was collected with a two-dimensional (2-D) Pilatus detector (**Figure 1b**) with an exposure time of 500 ms for each frame. Interferometry measurements were used simultaneously to observe changes in the layer thickness during drying.

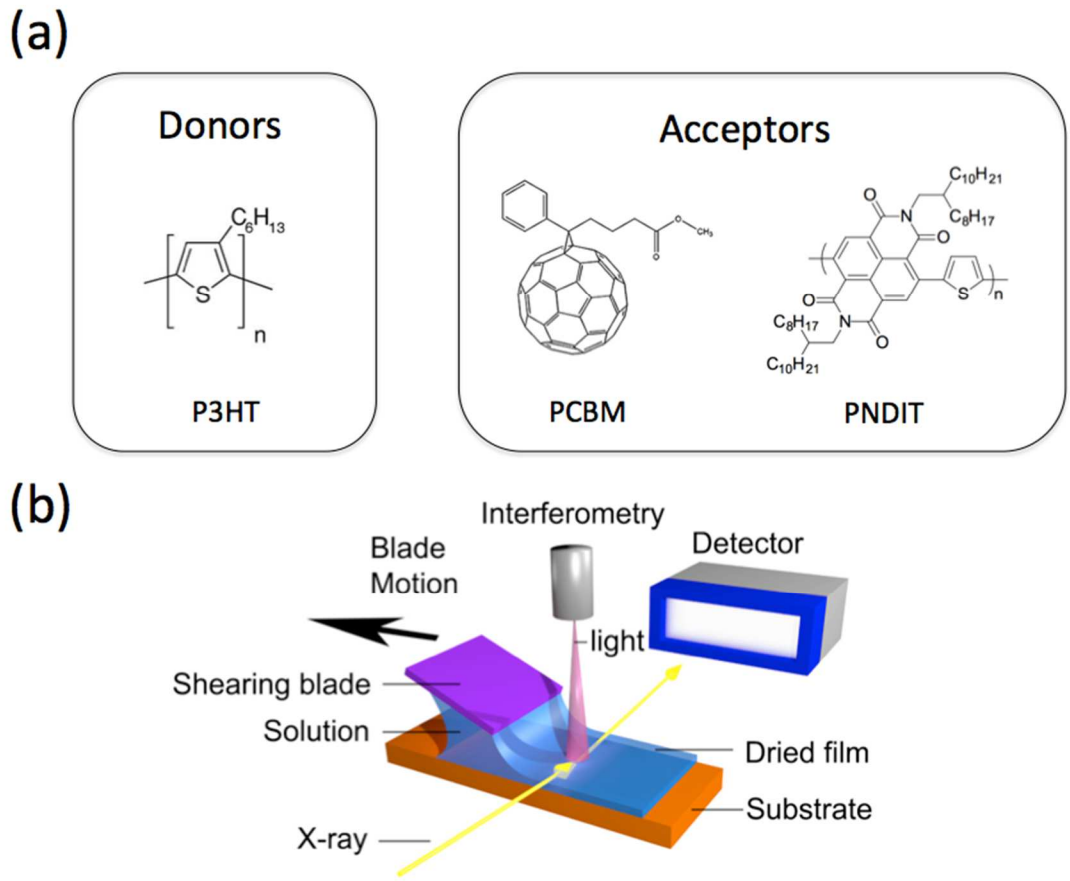


**Figure 1.** Structure of the donor and acceptor materials used in this study (a), and schematic drawing of real time X-ray scattering set-up (b).

In 2D grazing incidence X-ray diffraction, the incidence X-ray hits the sample surface at a shallow angle, then diffracts and is picked up by the area detector. The diffraction peaks carry the information about the packing structure of the polymeric chains. By carefully analyzing the diffraction pattern, crystallization processes of the conjugated polymer can be visualized. The detailed data reduction procedure is discussed in our previous publication.[47] In short, the (100) diffraction peaks are fitted with a Gaussian function with background to extract peak position, peak width and peak area. The peak position is inversely proportional to the alkyl chain packing distance (i.e. the distance between alkyl chain in polymer crystal) and the full width at half maximum (FWHM) is inversely related to the coherence length of polymer crystallites. Please note that the coherence length is proportional to, but not the exact same value as, the crystallite size. Because the coherence length estimated from the Scherrer equation did not fully consider corrections for the peak broadening due to instrumental settings or paracrystalline disorder[48]. Lastly, the integrated peak intensity is proportional to the total amount of polymer crystalline domains.

After fitting all the diffraction peaks, the film thickness, (100) alkyl chain packing peak position, FWHM and integrated peak intensity for P3HT in P3HT:PCBM and P3HT:PNDIT systems are plotted in **Figure 2**. The morphology evolution of P3HT (in the absence of acceptor) drying from chlorobenzene (CB) was first examined. We observed that the drying process of the polymer inks consisted of several different stages as shown in **Figure 2**. Those different stages, including: stage I (dissolved state), stage II (nucleation and growth), stage III (solvent swollen glassy state) and stage IV (glassy state), are colored to guide the eye. We performed the experiment on both P3HT ink (**Figure 2a**), P3HT:PCBM ink (**Figure 2b**), and P3HT:PNDIT ink (**Figure 2 c,d**). The detailed analyses of the different drying stages are presented in the following discussion.

As shown in **Figure 2a**, the morphology evolution of P3HT in CB includes several stages of drying. The initial wet film thickness was determined by solution viscosity, gap distance, and printing speed. Compared to P3HT:PCBM 1:1 ink, the P3HT ink has a higher viscosity and thus a thicker wet film (~11180 nm) was deposited immediately after printing. The constant decrease in layer thickness as function of time indicates a constant evaporation rate of the solvent (**See S-Figure 1**). During the first stage of drying **(Figure 2a** green region**)**, P3HT remained well-dissolved and no diffraction was observed. As the solvent continues to evaporate, the concentration of the polymer increases, and P3HT hit its solubility limit in chlorobenzene (at a concentration of 160 mg/ml with a wet film thickness of 2100 nm), followed by nucleation and crystallite growth, as signaled by the appearance of the (100) diffraction peak. In the second stage **(Figure 2a yellow** region**)**, the crystallization of P3HT continues as the ink continues to dry, and the diffraction peak intensifies. During the nucleation and growth stage (stage II), the (100) diffraction peak position initially appears at a value of 0.371 $A^{-1}$ (or a d-spacing of 1.69 nm given by Bragg's law), which is stable at first, and then increases slowly with time. We attribute this initial peak position to the formation of solvent-swollen nuclei. As the solvent continues to evaporate from the film, the packing distance between swollen alkyl chains decreases, as shown by the peak shift in stage II (**yellow** region). With ongoing solvent evaporation, the mobility of the P3HT chains in the CB solvent decreases. At stage III (solvent swollen glass state, **pink** region), the morphology evolution is affected by the polymer chain mobility, since the crystallization requires mass transport and rearrangement of polymer chains[49]. The polymer chain mobility can be understood by examining the glass transition temperature ($T_g$) of the solvent-swollen P3HT: CB domains. The $T_g$ describes the transition temperature for the polymer chain to transit from a glassy (frozen) to rubbery (flexible) state[50,51]. The CB solvent molecules can act as plasticizer to lower the glass transition temperature of the P3HT chains. As the solvent evaporates from the P3HT thin film, the $T_g$ for the polymer:solvent glass increases, and

consequently the polymer chain mobility decreases. Once the solvent evaporation throughout the polymer:solvent glass approaches completion, the mobility of the polymer chains is significantly reduced and exceeds the experimental time scale (~ hundreds of seconds). At this point the nucleation and growth process comes to an end (State II ended). The polymer chains was observed to be glassy when the film thickness dropped to 312 nm, by which the majority of the solvent had escaped from the sample, signaled by the plateauing of the integrated peak intensity **(Figure 2a** red region**)**. Because the polymer chains were in glassy state, there was no long-range rearrangement of the P3HT chains. During this Stage III, the peak intensity and FWHM remained unchanged, because no more polymer crystallites were formed or grown. The continued change in peak position was caused by reduction of the average packing distance between the alkyl chains as the residual solvent continued to escape from the film. Once all the residual solvent left the film, no further changes occurred and polymer thin film morphology was fixed, as shown in Stage IV **(Figure 2a** grey region**)**.

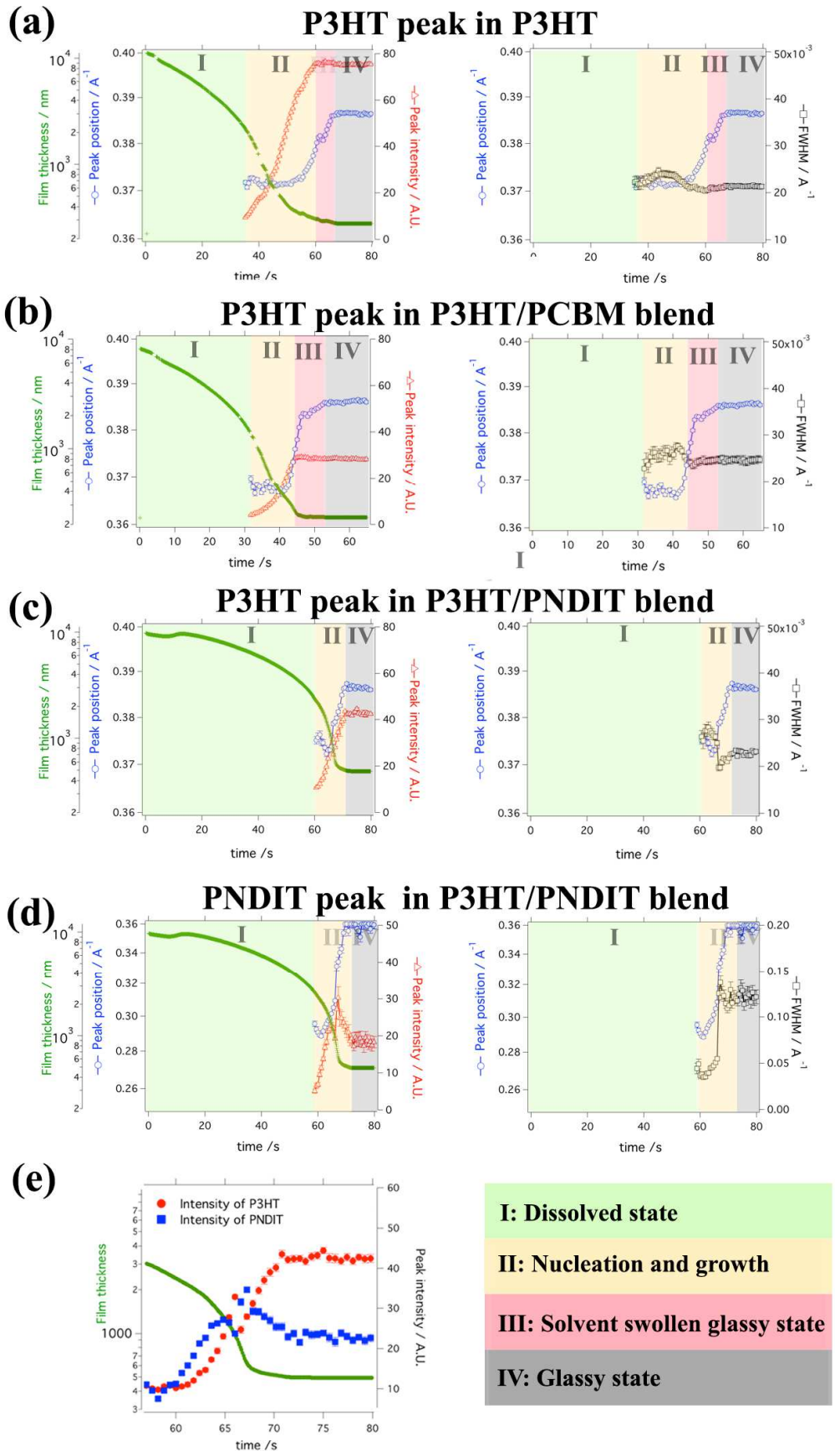
(a)
P3HT peak in P3HT
(b)
P3HT peak in P3HT/PCBM blend
(c)
P3HT peak in P3HT/PNDIT blend
(d)
PNDIT peak in P3HT/PNDIT blend
(e)
Film thickness / nm
Peak position / A^-1
Peak intensity / A.U.
FWHM / A^-1
time /s
I
II
III
IV
Intensity of P3HT
Intensity of PNDIT
I: Dissolved state
II: Nucleation and growth
III: Solvent swollen glassy state
IV: Glassy state

**Figure 2**: Evolution of the (100) diffraction peak of P3HT from P3HT ink (a), P3HT/PCBM 1:1 ink (b), P3HT/PNDIT 1:1 ink (c). Evolution of the (100) diffraction peak of PNDIT from P3HT/PNDIT 1:1 BHJ ink (d). The film thickness, integrated peak intensity and peak position are plotted in the left panel, and peak position and FWHM are plotted in the right panel. (e) Comparison of peak intensity P3HT (red) and PNDIT (blue) for P3HT:PNDIT cells in the late stage of drying. Different drying stages are marked with colors.

The crystallization of P3HT in P3HT:PCBM 1:1 weight ratio ink is very similar to the P3HT only ink. The addition of PCBM reduced the viscosity of the ink, resulting in thinner initial wet film of 8050 nm at the same coating speed and gap size as for neat P3HT. Same as the pure P3HT films, the drying behavior of P3HT:PCBM systems also consisted of the previously discussed four physical stages. Once the wet-film thickness reached 1270 nm (P3HT concentration of 95 mg/ml and a total solid concentration (P3HT:PCBM of 190 mg/ml), the P3HT polymer started to nucleate and grow (**Figure 2b** stage II yellow region). With decreasing film thickness (280 nm), the polymer chain and peak intensity stopped increasing with further drying (**Figure 2b** stage III pink region). The residual solvent continued to dry and peak position continued to increase, while the peak intensity and FWHM plateaued. The final dry film thickness was 230 nm (**Figure 2b** stage IV grey region). Our observation for P3HT:PCBM BHJ were confirmed by previous works. [34,36]

Compared to P3HT:PCBM, the morphology development for P3HT:PNDIT blends showed similar crystallization behavior during the early state of drying (Stage II, yellow region), but remarkable differences during the later stage **(Figure 2 c,d)**. When the wet-film thickness was reduced to 2160 nm (or at P3HT concentration of 66 mg/ml and a total solid concentration (P3HT:PNDIT) of 132 mg/ml), the P3HT polymer started to nucleate and grow (Stage II). Interestingly, Stage III (solvent swollen glass state, pink region) was not observed in the

drying process of P3HT:PNDIT ink. The intensity of P3HT (100) peak increased continuously until the film was fully dried (Stage IV, grey region). This morphology development was different from the drying process observed for the neat P3HT or P3HT:PCBM blend inks, where the peak intensity stopped increasing (Stage III) before the film was fully dried. These observations suggest that P3HT continues to crystallize even in the late stages of drying, when most of the solvent has already evaporated.

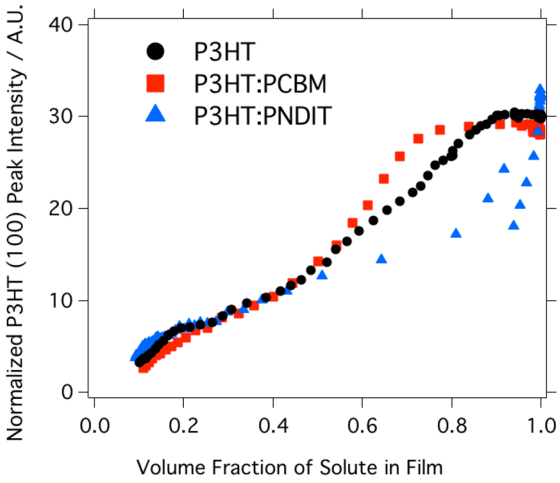


**Figure 3.** Plot of peak intensity for P3HT (100) vs solute concentration. The intensity of the P3HT diffraction peaks is normalized such that the intensity for the fully dried film is the same and arbitrarily set to 30. The solute volume fraction is normalized to 1 in fully dried state.

To better compare the three different drying processes, we plot the intensity of the P3HT (100) diffraction peak with respect to the normalized polymer concentration, as shown in **Figure 3**. The solute volume fraction, for both donor and acceptor, was obtained from the ratio of the dry film to swollen film thickness as measured by the real time interferometer. A polymer volume fraction of 1 indicates the film is fully dried and a solute volume fraction of 0.5 means the wet film consists half of the solute and half of the solvent. To simplify the process, here we assumed the same density for P3HT and CB. The crystallization for the

P3HT polymer stopped at a solute concentration of 0.75 for P3HT:PCBM blends compared to almost 1 for P3HT:PNDIT blends.

The different crystallization processes for P3HT in Figure 3 can be explained by the polymer chain mobility. When a liquid is cooled continuously, which happens during drying, the rate of diffusion decreases while the viscosity increases, reflecting a diminishing molecular mobility. Similarly, the glass transition in polymers occurs on cooling when the characteristic time of molecular motions responsible for structural rearrangements becomes longer than the timescale of the experiment. It is worth pointing out that, $T_g$ should not be treated as a physical constant, but as physical parameter that depends on the method of measurement. For example, $T_g$ shifts to a higher temperature with increasing cooling rates or measurement frequency[52]. The $T_g$ of a polymer blend system can be predicted by the classical Fox equation [53] or Kelley–Bueche equation[54]. To explain the observation in Figure 3, we estimated the $T_g$ for the P3HT:PCBM blend and P3HT:PNDIT blend using the Fox equation (**Equation 1**). Here, we do not intend to obtain the exact value of the $T_g$, but use the value to estimate the chain mobility.

$$\frac{1}{T_{g\,Mix}} = \frac{w_{polymer}}{T_{g\,polymer}} + \frac{w_{solvent}}{T_{g\,solvnt}} \quad (1)$$

$W_{polymer}$ and $W_{solvent}$ are the weight fractions of the polymer and solvent in the blend respectively. The $T_g$ of $PC_{61}BM$ was reported to be approximately 130 ˚C, and the $T_g$ of P3HT was reported to be 12 ˚C by differential scanning calorimetry (DSC)[55]. The $T_g$ of the PNDIT polymer was measured to be around -40 ˚C by DSC (See the Supporting Information **S-Figure 2**). The $T_g$ of conjugated polymer backbones is expected to be high (unlikely to be -40 ˚C) due to its rigid backbone. The observed $T_g$ around -40ºC must then be related to the alkyl side chains of the conjugated polymer, whereas the glass transition associated to the backbone is likely to be too weak to be observed in the DSC experiments due to limited sensitivity. It

has been previously noted that long alkyl chains could have their own $T_g$[56]. The $T_g$ value obtained from the Fox equation is a rough of the chain mobility. According to the Fox equation, the hypothetical $T_g$ of an amorphous phase of 1:1 blend of PNDIT and P3HT, if exists, was is estimated to be -14 ˚C[53]. As a result, the 1:1 mixture of P3HT:PNDIT blend with a $T_g$ of -14 ˚C would be probably able to crystallize at 35 ˚C even with most of the solvent evaporated. On the other hand, the 1:1 blend of P3HT:PCBM showed a much higher $T_g$ of 71.5 ˚C predicted by Equation 1 , which prevented the polymer from crystallizing further at 35 ˚C within experimental time scale. Various groups have also observed elevated $T_g$ for P3HT:PCBM blends as compared to P3HT, using DSC[55], real time X-ray diffraction[57], DMA[58], ellipsometry[59], and in operando measurement of the solar cell at different temperatures[60].

The diffraction of the PNDIT polymer was also analyzed for P3HT:PNDIT polymer blend. The (100) diffraction peak from the PNDIT polymer is shown in **Figure 1d**. Previous real time X-ray scattering work based on P3HT:PCBM was not able to analyzed the scattering peak from acceptors due to the low diffraction signal from PCBM, as well as overlapping peak position with halogenated solvent scattering[36,38,40]. Longer exposure time, ~10s could improve the diffraction intensity from PCBM but sacrifices the frame rates[39]. In contrast, the PNDIT polymer has strong diffraction peaks and is therefore chosen to give insights into the crystallization process of acceptor polymers. The diffraction peak for PNDIT showed up at a wet film thickness of ~2410 nm. The acceptor polymer crystallized at a concentration of 60 mg/ml or a total of solid concentration of 120 mg/ml, which was slightly lower than that of the donor polymer **(Figure 2e)**. This shows that the acceptor polymer crystalized first to form aggregates, which serves as the initial driving force for the blend system to phase separate[43]. The intensity of the PNDIT (100) diffraction peak initially increased then decreased, which contrasts to ever-growing P3HT peak. The onset for this decrease coincides with the increase

of the intensity of the P3HT (100) peak. We speculate that the crystallization of the P3HT induces disorder in the previous formed PNDIT domains, possibly because the PNDIT chains were still allowed to move because its $T_g$ was below room temperature.

Further quantitative structural information of the crystalline domains in the dried film has been obtained using *ex situ* GIWAXS with a large-area detector. In order to understand the phase behavior between two polymers, the blend ratio between the donor and acceptor polymer was systematically varied from 9:1, 7:3, 5:5, 3:7 to 1:9 by weight. The *ex situ* samples were prepared at beamline with the same sample preparation protocol to ensure the same sample morphology from the *in situ* experiments. The *ex situ* GIWAXS diffraction images for P3HT:PCBM and P3HT:PNDIT blends at those blend ratios are presented in **Figure 4**.

For the 9:1 P3HT:PCBM blend, the P3HT polymer showed a similar diffraction pattern compared to the pure P3HT sample (See Supporting Information **S-Figure 3**)). As the PCBM concentration is increased (holding total solute concentration constant), the P3HT (100) diffraction peak intensity decreases, while the scattering intensity for PCBM increases. At a 3:7 blend ratio, only a very weak (100) diffraction peak from P3HT was observed. No diffraction peak from P3HT was observed when in 1:9 blend ratio, indicating that all the P3HT adopted an amorphous phase or intermixed with PCBM. The miscibility between P3HT (regioregular) and PCBM was estimated to be around 20% from **Figure 4c**. This is in agreement with observations from literature that P3HT and PCBM have partial miscibility[61-64].

For P3HT:PNDIT, (**Figure 4c**), the diffraction signal from PNDIT was already observable even in the 9:1 blend and the peak intensified with higher acceptor content. More interestingly,

in contrast to the P3HT:PCBM blends, the (100) peak of P3HT was persistently observed even at 1:9 blend ratio. This indicates that the P3HT donor and PNDIT acceptor polymers have a strong tendency to phase separate (low miscibility), in contrast to the relatively high miscibility between P3HT and PCBM.

Using the (200) diffraction peak, the amount of P3HT crystalline domain was calculated and plotted in **Figure 4c** for different systems. The (200) peak was chosen over (100) to avoid the interference with specular X-ray from grazing incidence geometry. The integrated diffraction signal was normalized by incidence beam intensity, exposure time, film thickness and beam path. The amount of pure crystalline P3HT, as extracted from P3HT diffraction peak followed a linear trend with respect to the blend ratio for both blend systems, although it decreased faster with increased contents of PCBM than that of PNDIT. Moreover, for the 1:1 blend ratio, the P3HT peak intensity is 40% higher in P3HT:PNDIT blend compared to that in the P3HT:PCBM blend. This is likely due to the stronger tendency for the P3HT to mix with PCBM to form P3HT:PCBM mixed glassy domains with high $T_g$ as observed by real-time X-ray diffraction experiments. There is less mixed phase for all polymers BHJ in this case as see from **Figure 4c**.

The alkyl chain packing distance and π-π stacking distances for P3HT were analyzed, revealing no significant differences for the different blend ratios (See Supporting Information Table 1). The P3HT crystal showed an alkyl packing distance of 16.6 ± 0.02 $Å^{-1}$, and a π-π packing distance of 3.75 ± 0.02 $Å^{-1}$. The observed values agree with previous observations by other groups[32,57,65]. This indicates that both acceptors do not form crystalline domain with P3HT donor.

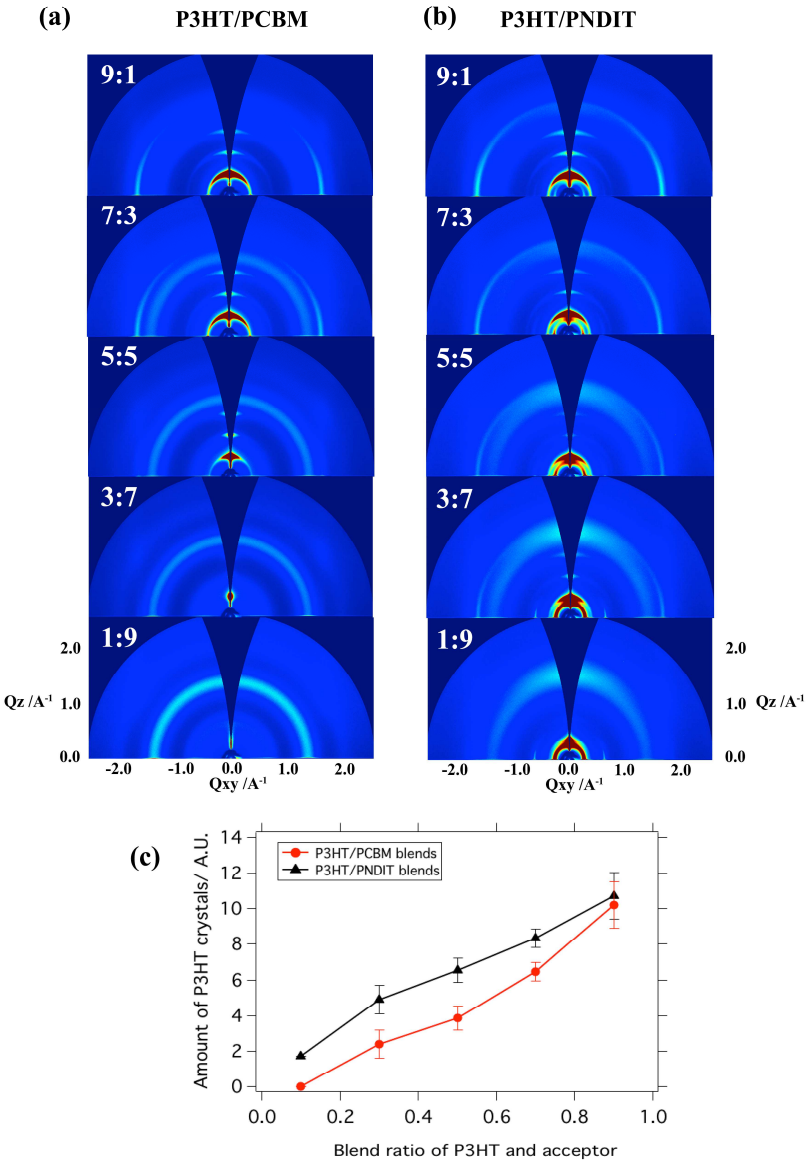


**Figure 4,** GIWAXS diffraction pattern of the P3HT/PCBM (a) and P3HT/PNDIT (b) blends system. Amount of pure crystalline P3HT with different blend ratios (c). The total integrated peak intensity was normalized to film thickness, exposure time and beam path for a fair comparison.

In order to further understand how different acceptors impact the phase separation in P3HT:PCBM and P3HT:PNDIT blend films, we employed transmission electron microscopy (TEM) and atomic force microscopy (AFM) for real-space imaging of the film morphology

(See **S-Figure** 4 & 5, respectively). TEM showed that for the samples with blend ratio of 1:1, the P3HT:PNDIT film exhibited a network-like highly phase separated morphology with length scale around hundreds of nanometers to one micron, in contrast to visually more uniform film seen from P3HT:PCBM images. By probing the top surface morphology, AFM showed that the blend films made from P3HT:PCBM had a smoother surface and indicated that the large scale phase separation seen with TEM is likely from the film thickness variation. Due to the low electron density difference between the donor and acceptor materials when thickness variation is not as large for other blend ratios, TEM could not provide sufficient in-sight information on the phase separation. Therefore, we employed resonant soft X-ray scattering (RSoXS) with X-ray energies around carbon K absorption edge, with which the contrast between donor and acceptor in the blend film is greatly enhanced [66,67].

For P3HT:PCBM blends (**Figure 5a**), the X-ray energy of 284.2 eV was used for best scattering contrast between the two constituents. Mostly isotropic scattering patterns were observed for all blend ratios. A bimodal distribution of the scattering intensity vs scattering vector Q was observed for high P3HT:PCBM ratio, especially for the 7:3 blend. As the blend ratio of P3HT:PCBM decreases from 9:1 to 1:9, the X-ray scattering intensity distribution became a singe peak and shifted to higher q. For P3HT:PCBM with 5:5 blend ratio, a reasonably strong scattering peak at q = 0.03 $Å^{-1}$ was observed, which corresponds to a domain-domain spacing of around 21 nm. When the PCBM concentration was further increased, the domain spacing was further reduced down to 18nm for 3:7 blend ratio and less than 9 nm for 1:9 blend ratio. This is likely due to the early lock-in of the amorphous domains resulting from increased $T_g$ of amorphous P3HT:PCBM blends for the higher blending ratio of PCBM (the $T_g$ of the 3:7 P3HT:PCBM blend is predicted to be 86.0 ˚C, and the $T_g$ of the 1:9 P3HT:PCBM is predicted to be 114.8 ˚C using the Fox equation as shown Equation 1). The increased $T_g$ causes a reduction in the P3HT chain mobility, since the substrate temperature was fixed at 35°C. As a result, 1:9 blend P3HT:PCBM will freeze in P3HT crystallization at

an early drying stage, by forming higher fraction of glassy mixture of P3HT:PCBM, hence slightly smaller phase separation.

In contrast, for P3HT:PNDIT blends, most of the intensity is concentrated in the low q region, which indicates a much larger phase separation between donors and acceptors. Slight scattering anisotropy was observed when comparing the scattering profiles parallel and perpendicular to the beam polarization direction. This anisotropy was insensitive to sample in-plane rotation, indicating that the polymer chains have local correlation in their orientation alignment (over tens of nanometers), but are globally isotropic[68]. As the blend ratio of P3HT:PDNIT changed from 9:1 to 1:9, the scattering pattern showed different trends when compared to P3HT:PCBM blends. For 1:1 blend ratio, a decay of scattering intensity vs scattering vector was observed. Combined with the observations by TEM imaging, we would expect a weak scattering peak at smaller scattering vector than accessed (at $q < 0.001$ $Å^{-1}$ or a domain-domain spacing >628nm). This is also evidenced by optical microscope imaging (**See S-Figure 6**) and AFM showing large phase scale separation (**See S-Figure 5**). Such large scales were likely not due to crystallization-induced phase separation but more likely due to the spinodal decomposition of donor and acceptor phases[69]. Another very weak scattering intensity hump was observed at the high scattering vector region. The scattering peak at the high q region, which corresponds to a size scale of 20 nm, was insensitive to the composition change, which we attribute to the P3HT domains, perhaps P3HT crystallites. This is consistent within the experimental error with the observation of ex-situ GIWAXS, where the coherence length for the crystalline domain of P3HT polymer was observed to be about 12nm as estimated from Scherrer equation[70] and a value of FWHM ~0.024 $A^{-1}$. A peak in I(Q) with a scattering vector of 0.002 $Å^{-1}$ was observed for both the 1:9 and 9:1 blend ratio. Those two peaks correspond to a size scale of ~300 nm, which we believe is from the surface roughness due to large phase separation. The same peaks at the low q value were also observed at the

beam energy of 270eV, which we used to maximize the contrast between the layer and vacuum, which is sensitive to surface roughness (**S-Figure 7**).

A comparison of the P3HT:PCBM blend with P3HT:PNDIT blend showed that the phase separation size scale was much smaller for the polymer:fullerene blend. Furthermore, the phase-segregation scale for polymer: fullerene blend becomes smaller with an increase of the fullerene content, which agrees well with observed intermix between P3HT and PCBM from *ex situ* GIWAXS data, since the crystallization is the driving force for the phase separation process. On the other hand, the polymer:polymer blend showed similar small phase separation at 20 nm as well as large phase separation (μm scale), due to the crystallization induced phase separation as well as the spinodal decomposition.

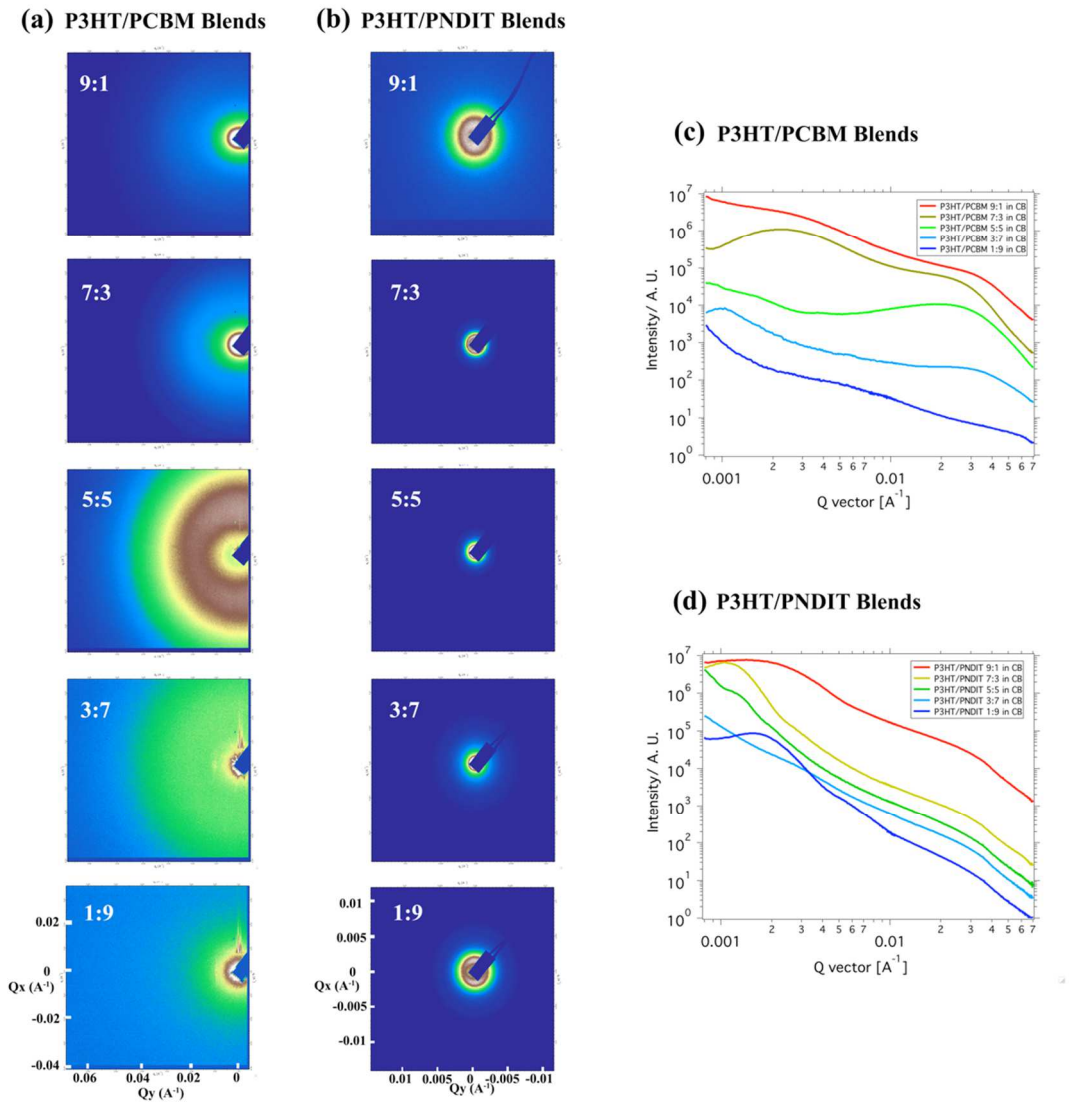


**Figure 5:** the RSoXS scattering of the P3HT:PCBM solar cells (284.2 eV) (a) and P3HT:PNDIT solar cell with different blend ratio (285.2 eV) (b) . The intensity vs scattering vector is shown in (c) P3HT:PCBM and (d) P3HT:PNDIT

On the basis of our results above, we propose the following process for the morphology evolution of the donor and acceptor phases and discuss the differences between the polymer acceptor and fullerene acceptor (Figure 6). In Stage I of the drying process, the donor and acceptor are well dissolved in the solution. As solvent evaporation proceeds, the concentration of solute goes up. Once the critical concentration is reached, the crystallization occurs (Stage

II and III), either from donor or acceptor. The nucleation and growth of the polymer chains continues until they are frozen, due to increased $T_g$ in solvent swollen polymer glass. For the polymer:fullerene:solvent glass, the glass transition temperature is higher due to high $T_g$ of the PCBM component, and thus arrests the crystallization and phase separation at an early stage of the drying process. As a result, a small phase separation between the P3HT and PCBM by RSoXS and 20% amorphous mixture of P3HT and PCBM were observed by ex situ GIWAXS. On the other hand, during the drying process, the intermediate state of intermixed region in the solvent for the polymer/polymer system showed a $T_g$ lower than room temperature. Therefore, donor and acceptor polymers further crystallized, which results in a large phase separation and a detrimental impact on the charge separation process.

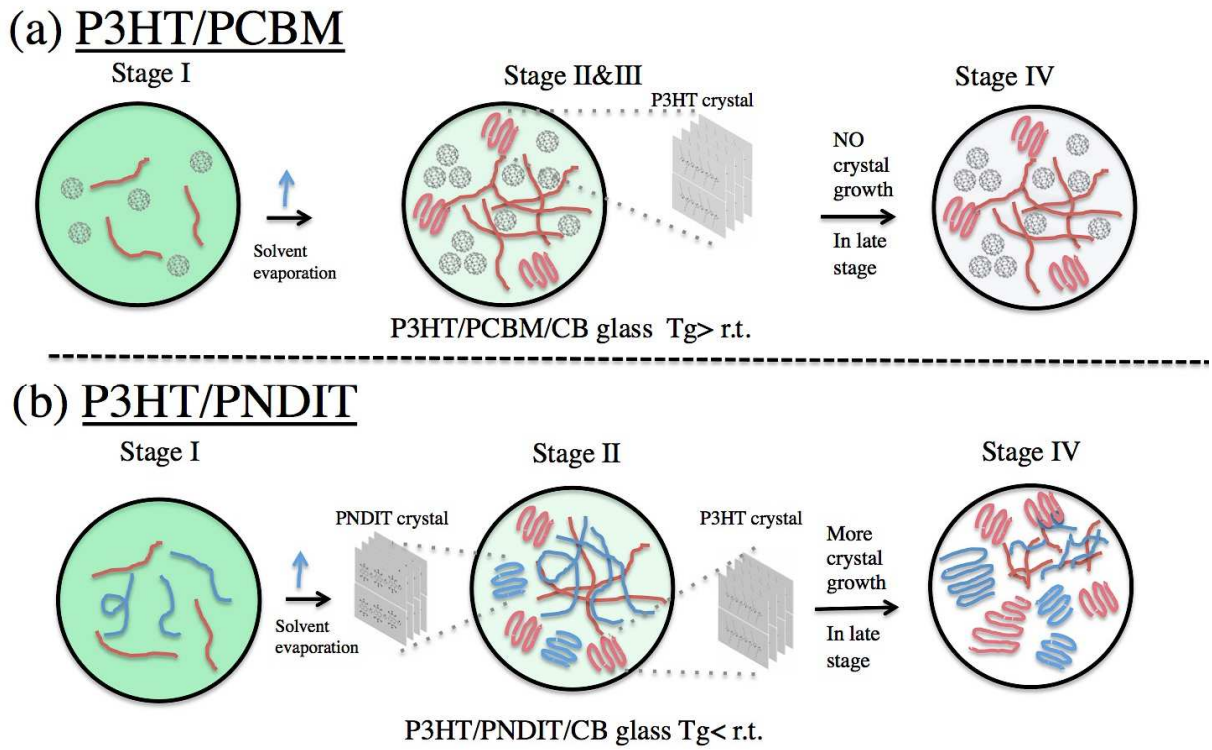


**Figure 6**: schematic of the drying process for polymer:fullerene (a) and polymer:polymer (b) solar cells. With polymer/PCBM blend, a smaller phase separation is formed due to the high

$T_g$ of the mixture of P3HT/PCBM. The red chains represent P3HT, the blue chains represent PNDIT, black dots represent PCBM, and the green represents solvent.

To test whether the proposed process in Figure 6 is applicable to other materials, we performed experiments with another donor polymer, polyisoindigo bithiophene (PiI-2T), with PCBM or PNDIT acceptor. Similarly, we observed a large phase separation for PiI-2T:PNDIT blends (600 nm) compared to PiI-2T:PCBM blends (150 nm) (see **S-Figure 8**). This observation agrees well with results from P3HT:PCBM blends discussed above.

As discussed above, the all polymer solar cells studied here show strong tendency to phase separate into large domains. Thus, to reduce domain size, it is worth considering two different routes. The first is to use high $T_g$ donors and acceptors, and to trap the donors and acceptors into intermixed phase to form smaller phase separation[51]. Moreover, a high $T_g$ active layer is also desired for long term thermal stability of solar cell[71]. There are several reports on highly stable OPV by using high $T_g$ donors or acceptors. For example, poly[2-methoxy-5- (30,70-dimethyloctyloxy)-1,4-phenylene vinylene] (MDMO-PPV), which has a $T_g$ of ~138 °C, has shown improved thermal stability compared to P3HT based polymer:fullerene solar cells[72]. The $T_g$ of a polymer depends on the molecular weight of polymer as described by the Flory-Fox equation[73]. Increasing polymers' molecular weight not only benefits from smaller phase separation from elevated $T_g$, but also improved charge carrier mobility to enhance charge extraction[65]. There are also high $T_g$ acceptors. For example, the $PC_{71}BM$ has a $T_g$ of 163 °C and indene C60 bis-adduct (ICBA) has a $T_g$ of 168 °C[74]. Instead from reducing phase separation from by kinetics, another route is to control the mixing energy between two polymers based on the thermodynamics. The classical Flory-Huggins theory was developed for mixing of two-polymer melts. The interaction between two polymers can be simplified to the Flory Huggins parameter $\chi$, which can be

calculated from the solubility parameter of the respective polymers. If one can measure the solubility parameter, the mixing energy between two polymers could be estimated. Several groups have reported the measurement of the solubility parameter by either the ellipsometry[74] or the solvent swelling experiment[75]. It is important to reduce the interaction pair between the donors and acceptors to form mixed phase, which has been shown to form new energy landscape that may be very important for high performance solar cells[76,77].

Conclusion:

In summary, we use real-time X-ray scattering to compare the morphology development of the P3HT donor polymer when blended with PCBM or PNDIT acceptor polymers. In contrast to PCBM, PNDIT has a lower tendency to form a mixed phase with P3HT than PCBM, which may be the key to inhibit the donor polymer crystallization process, thus creating preferred small phase separation between the donor and acceptor polymer.

For future development of all-polymer solar cells, consideration for donor/acceptor crystallization behavior is needed to prevent the BHJ from forming large phase separation, which hinders the exciton splitting at the interface. Thus, to reduce the large phase separation occurring during fabrication of all solar cells, the crystallization of the donor and acceptor polymers needs to be suppressed, especially for highly crystalline polymers. This highlights the need to consider tuning the polymer's ability to crystalize (or aggregate) during the drying process.

**Experimental Section**

*Materials.* Regioregular P3HT (Sepiolid P100, by BASF in cooperation with Rieke, molecular weight of $M_n$ = 12,480 g/mol and a polydispersity index of 1.7 was used. $C_{61}$PCBM was obtained from Nano-C. Both materials were used as received. The naphthalene diimide

thiophene acceptor copolymer (PNDIT) was synthesized according to previously reported procedures[78]. The number average molecular weight ($M_n$) and weight dispersity ($Đ_W$) measured by high temperature size exclusion chromatography (HT-SEC) were 28.2 kDa and 1.8, respectively. HT-SEC using 1,2,4-trichlorobenzene was performed at 180 °C on a Tosoh High-temperature EcoSEC equipped with a single TSKgel GPC column (GMHHR-H; 300 mm × 7.8 mm) calibrated by monodiperse polystyrene standards. DSC experiments were carried out with a TA Instruments DSC Q2000 using Tzero Aluminum pans.

*Morphology characterizations.* In situ X-ray scattering during the solvent evaporation was performed at Beamline 7-2 of the Stanford Synchrotron Radiation Lightsource (SSRL) with a two-dimensional area Pilatus detector (Dectris, 300k). The sample to detector distance was 386.2 mm, and the incidence angle was 0.12°. The X-ray wavelength was 0.8266 Å, corresponding to an X-ray beam energy of 15 keV. The X-ray beam flux was attenuated by a factor of 30 to reduce beam damage to the sample. In situ film thickness was monitored by a Filmetrics F-20 EXR interferometer equipped with an infrared light source. The infrared spectrum on the drying sample was acquired every 100 ms. The data points were then analyzed using the software provided by Filmetric to extract the film thickness.

Ex situ grazing incidence wide angle X-ray scattering (GIWAXS) was performed at Beamline 11-3 of the SSRL with a two-dimensional area detector (Mar345 Image Plate) and the sample in a helium atmosphere. The sample to detector distance was 400 mm, and the incidence angle was 0.12˚. The X-ray wavelength was 0.9758 Å, corresponding to an X-ray beam energy of 12.7 keV.

Ex situ resonant soft X-ray scattering (RSoXS) data were collected at the Advanced Light Source (ALS) Beamline 11.0.1.2 in transmission geometry inside a high vacuum chamber[79].

For sample preparation, Si wafers with native oxides were first treated in ultraviolet-ozone for 20 min followed by spin-coating of poly(sodium 4-styrenesulfonate) from a 10 wt% aqueous solution at 5,000 rpm for 30 s. The substrates were then baked in air at 80 ˚C for 10 min to remove residual water. The polymer solar cell thin films were solution printed on the poly(sodium 4-styrenesulfonate)-coated Si wafer with the same process condition used in the real-time X-ray scattering experiment, and then floated off in deionized water and transferred to a 100 nm $Si_3N_4$ membrane supported on a 5 by 5 mm, 200-um-thick Si frame (Norcada Inc.). The film was then dried in air before being transferred into the vacuum chamber for RSoXS. The beam energy was swept from 270 to 290 eV, with a 10 s exposure time per scan. Scattering patterns were collected on a two-dimensional charge-coupled device camera in vacuum and cooled to -45 ˚C (Princeton Instrument PI-MTE). Diffraction data were collected at two sample to detector distances of 50mm and 150mm respectively, to give a combined q range of 0.001 ~ 0.070 $Å^{-1}$. Data analysis was performed using the Nika package supported in the Igor Pro environment[80].

**Supporting Information**
Supporting Information is available from the Wiley Online Library or from the author.

**Acknowledgements**
X.G., Y.Z., M.T., and Z.B. acknowledge support through the Bridging Research Interactions through collaborative the Development Grants in Energy (BRIDGE) program under the SunShot initiative of the Department of Energy program under contract DE-FOA-0000654-1588. T.K. and Z.B. acknowledge support from the Office of Naval Research (□□□□□□□□□□□□□□□□□□). K.G. was supported by the Department of Defense (DoD) through the National Defense Science & Engineering Graduate Fellowship (NDSEG) Program. H.Y. acknowledges support from the National Science Foundation Materials Genome Program (Award no. 1434799). B.S. acknowledges the National Research Fund of

Luxembourg for financial support (Project 6932623). F.M.-L. acknowledges the Swiss National Science Foundation (Award no. P2ELP2_155355). *In situ* measurements were carried out at the Stanford Synchrotron Radiation Laboratory, a national user facility operated by Stanford University on behalf of the U.S. Department of Energy, Office of Basic Energy Sciences, under Contract No. DE-AC02-76SF00515. RSoXS experiments were performed at Advanced Light Source, which is supported by the Director, Office of Science, Office of Basic Energy Sciences, of the U.S. Department of Energy under Contract No. DE-AC02-05CH11231. We thank Bart Johnson for assistance during the in situ experiment at SSRL Beamline 7-2. Nathan Ging-Ji Wang for performing the high-temperature SEC experiments.

Received: ((will be filled in by the editorial staff))
Revised: ((will be filled in by the editorial staff))
Published online: ((will be filled in by the editorial staff))

[1] J. Zhao, Y. Li, G. Yang, K. Jiang, H. Lin, H. Ade, W. Ma, H. Yan, *Nat. Energy* **2016**, *1*, 15027.
[2] W. Zhao, D. Qian, S. Zhang, S. Li, O. Inganäs, F. Gao, J. Hou, *Adv. Mater.* **2016**, n.
[3] A. Facchetti, *Materials Today* **2013**, *16*, 123.
[4] T. Kim, J.-H. Kim, T. E. Kang, C. Lee, H. Kang, M. Shin, C. Wang, B. Ma, U. Jeong, T.-S. Kim, B. J. Kim, *Nat Commun* **2015**, *6 SP* -, 1.
[5] J. Liu, S. Chen, D. Qian, B. Gautam, G. Yang, J. Zhao, J. Bergqvist, F. Zhang, W. Ma, H. Ade, O. Inganäs, K. Gundogdu, F. Gao, H. Yan, *Nat. Energy* **2016**, *1*, 16089 EP.
[6] S. Li, H. Zhang, W. Zhao, L. Ye, H. Yao, B. Yang, S. Zhang, J. Hou, *Adv. Energy Mater.* **2015**, n.
[7] Y. Zhou, T. Kurosawa, W. Ma, Y. Guo, L. Fang, K. Vandewal, Y. Diao, C. Wang, Q. Yan, J. Reinspach, J. Mei, A. L. Appleton, G. I. Koleilat, Y. Gao, S. C. B. Mannsfeld, A. Salleo, H. Ade, D. Zhao, Z. Bao, *Adv. Mater.* **2014**, *26*, 3767.
[8] E. Zhou, J. Cong, Q. Wei, K. Tajima, C. Yang, K. Hashimoto, *Angew. Chem. Int. Ed.* **2011**, *50*, 2799.
[9] X. Zhan, Z. Tan, B. Domercq, Z. An, X. Zhang, S. Barlow, Y. Li, D. Zhu, B. Kippelen, S. R. Marder, *J. Am. Chem. Soc.* **2007**, *129*, 7246.
[10] C. Lee, H. Kang, W. Lee, T. Kim, K.-H. Kim, H. Y. Woo, C. Wang, B. J. Kim, *Adv. Mater.* **2015**, *27*, 2466.
[11] Y.-J. Hwang, B. A. E. Courtright, A. S. Ferreira, S. H. Tolbert, S. A. Jenekhe, *Adv. Mater.* **2015**, *27*, 4578.
[12] E. Zhou, M. Nakano, S. Izawa, J. Cong, I. Osaka, K. Takimiya, K. Tajima, *ACS Macro Lett.* **2014**, *3*, 872.
[13] J. Choi, K.-H. Kim, H. Yu, C. Lee, H. Kang, I. Song, Y. Kim, J. H. Oh, B. J. Kim, *Chem. Mater.* **2015**, *27*, 5230.

[14] H. Kang, K.-H. Kim, J. Choi, C. Lee, B. J. Kim, *ACS Macro Lett.* **2014**, *3*, 1009.
[15] S. Nam, S. Woo, J. Seo, W. H. Kim, H. Kim, C. R. McNeill, T. J. Shin, D. D. C. Bradley, Y. Kim, *ACS Appl. Mater. Interfaces* **2015**, *7*, 15995.
[16] J. W. Jung, J. W. Jo, C.-C. Chueh, F. Liu, W. H. Jo, T. P. Russell, A. K. Y. Jen, *Adv. Mater.* **2015**, *27*, 3310.
[17] D. Mori, H. Benten, I. Okada, H. Ohkita, S. Ito, *Energy Environ. Sci.* **2014**, *7*, 2939.
[18] S. Fabiano, Z. Chen, S. Vahedi, A. Facchetti, B. Pignataro, M. A. Loi, *J. Mater. Chem.* **2011**, *21*, 5891.
[19] Z. He, C. Zhong, S. Su, M. Xu, H. Wu, Y. Cao, *Nat Photon* **2012**, *6*, 591.
[20] N. Zhou, H. Lin, S. J. Lou, X. Yu, P. Guo, E. F. Manley, S. Loser, P. Hartnett, H. Huang, M. R. Wasielewski, L. X. Chen, R. P. H. Chang, A. Facchetti, T. J. Marks, *Adv. Energy Mater.* **2013**, *4*, n.
[21] M. Schubert, D. Dolfen, J. Frisch, S. Roland, R. Steyrleuthner, B. Stiller, Z. Chen, U. Scherf, N. Koch, A. Facchetti, D. Neher, *Adv. Energy Mater.* **2012**, *2*, 369.
[22] H. Yan, B. A. Collins, E. Gann, C. Wang, H. Ade, C. R. McNeill, *ACS Nano* **2012**, *6*, 677.
[23] B. R. Gautam, C. Lee, R. Younts, W. Lee, E. Danilov, B. J. Kim, K. Gundogdu, *ACS Appl. Mater. Interfaces* **2015**, *7*, 27586.
[24] J. M. Hodgkiss, A. R. Campbell, R. A. Marsh, A. Rao, S. Albert-Seifried, R. H. Friend, *Phys. Rev. Lett.* **2010**, *104*, 177701.
[25] J. R. Moore, S. Albert-Seifried, A. Rao, S. Massip, B. Watts, D. J. Morgan, R. H. Friend, C. R. McNeill, H. Sirringhaus, *Adv. Energy Mater.* **2011**, *1*, 230.
[26] H. Benten, T. Nishida, D. Mori, H. Xu, H. Ohkita, S. Ito, *Energy Environ. Sci.* **2016**, *9*, 135.
[27] L. Gao, Z.-G. Zhang, L. Xue, J. Min, J. Zhang, Z. Wei, Y. Li, *Adv. Mater.* **2016**, *28*, 1884.
[28] F. Liu, Y. Gu, X. Shen, S. Ferdous, H.-W. Wang, T. P. Russell, *Progress in Polymer Science* **2013**, *38*, 1990.
[29] W. Chen, M. P. Nikiforov, S. B. Darling, *Energy Environ. Sci.* **2012**, *5*, 8045.
[30] J. Rivnay, S. C. B. Mannsfeld, C. E. Miller, A. Salleo, M. F. Toney, *Chem. Rev.* **2012**, *112*, 5488.
[31] Y. Huang, E. J. Kramer, A. J. Heeger, G. C. Bazan, *Chem. Rev.* **2014**, *114*, 7006.
[32] D. Chen, A. Nakahara, D. Wei, D. Nordlund, T. P. Russell, *Nano Lett.* **2011**, *11*, 561.
[33] D.-M. Smilgies, R. Li, G. Giri, K. W. Chou, Y. Diao, Z. Bao, A. Amassian, *Phys. Status Solidi RRL* **2012**, *7*, 177.
[34] S. Pröller, F. Liu, C. Zhu, C. Wang, T. P. Russell, A. Hexemer, P. Müller-Buschbaum, E. M. Herzig, *Adv. Energy Mater.* **2016**, *6*, n.
[35] J. T. Rogers, K. Schmidt, M. F. Toney, G. C. Bazan, E. J. Kramer, *J. Am. Chem. Soc.* **2012**, *134*, 2884.
[36] L. J. Richter, D. M. DeLongchamp, F. A. Bokel, S. Engmann, K. W. Chou, A. Amassian, E. Schaible, A. Hexemer, *Adv. Energy Mater.* **2015**, *5*, n.
[37] S. Engmann, F. A. Bokel, A. A. Herzing, H. W. Ro, C. Girotto, B. Caputo, C. V. Hoven, E. Schaible, A. Hexemer, D. M. DeLongchamp, L. J. Richter, *J. Mater. Chem. A* **2015**, *3*, 8764.
[38] F. Liu, S. Ferdous, E. Schaible, A. Hexemer, M. Church, X. Ding, C. Wang, T. P. Russell, *Adv. Mater.* **2014**, *27*, 886.
[39] A. J. Pearson, T. Wang, A. D. F. Dunbar, H. Yi, D. C. Watters, D. M. Coles, P. A. Staniec, A. Iraqi, R. A. L. Jones, D. G. Lidzey, *Adv. Funct. Mater.* **2013**, *24*, 659.
[40] B. Schmidt-Hansberg, M. Sanyal, M. F. G. Klein, M. Pfaff, N. Schnabel, S. Jaiser, A. Vorobiev, E. Müller, A. Colsmann, P. Scharfer, D. Gerthsen, U. Lemmer, E. Barrena, W. Schabel, *ACS Nano* **2011**, *27*, 8579.

[41] M. Sanyal, B. Schmidt-Hansberg, M. F. G. Klein, A. Colsmann, C. Munuera, A. Vorobiev, U. Lemmer, W. Schabel, H. Dosch, E. Barrena, *Adv. Energy Mater.* **2011**, *1*, 363.
[42] M. Sanyal, B. Schmidt-Hansberg, M. F. G. Klein, C. Munuera, A. Vorobiev, A. Colsmann, P. Scharfer, U. Lemmer, W. Schabel, H. Dosch, E. Barrena, *Macromolecules* **2011**, *44*, 3795.
[43] K. W. Chou, B. Yan, R. Li, E. Q. Li, K. Zhao, D. H. Anjum, S. Alvarez, R. Gassaway, A. Biocca, S. T. Thoroddsen, A. Hexemer, A. Amassian, *Adv. Mater.* **2013**, *25*, 1923.
[44] G. Giri, E. Verploegen, S. C. B. Mannsfeld, S. Atahan-Evrenk, Do Hwan Kim, S. Y. Lee, H. A. Becerril, A. Aspuru-Guzik, M. F. Toney, Z. Bao, *Nature* **2011**, *480*, 504.
[45] G. Giri, D. M. DeLongchamp, J. Reinspach, D. A. Fischer, L. J. Richter, J. Xu, S. Benight, A. Ayzner, M. He, L. Fang, G. Xue, M. F. Toney, Z. Bao, *Chem. Mater.* **2015**, *27*, 2350.
[46] G. Giri, R. Li, D.-M. Smilgies, E. Q. Li, Y. Diao, K. M. Lenn, M. Chiu, D. W. Lin, R. Allen, J. Reinspach, S. C. B. Mannsfeld, S. T. Thoroddsen, P. Clancy, Z. Bao, A. Amassian, *Nat Commun* **2014**, *5 SP* -, 1.
[47] X. Gu, J. Reinspach, B. J. Worfolk, Y. Diao, Y. Zhou, H. Yan, K. Gu, S. Mannsfeld, M. F. Toney, Z. Bao, *ACS Appl. Mater. Interfaces* **2016**, *8*, 1687.
[48] R. Noriega, J. Rivnay, K. Vandewal, F. P. V. Koch, N. Stingelin, P. Smith, M. F. Toney, A. Salleo, *Nat Mater* **2013**, *12*, 1038.
[49] G. Reiter, *Chem. Soc. Rev.* **2014**, *43*, 2055.
[50] J. H. Gibbs, E. A. DiMarzio, *J. Chem. Phys.* **1958**, *28*, 373.
[51] C. Müller, *Chem. Mater.* **2015**, *27*, 2740.
[52] J. A. Forrest, K. Dalnoki-Veress, *Advances in Colloid and Interface Science* **2001**, *94*, 167.
[53] T. G. Fox, *Influence of diluents and of copolymer composition on the glass temperature of a polymer system*; Bull Am Phys Soc, 1956.
[54] F. N. Kelley, F. Bueche, *Journal of Polymer Science* **2003**, *50*, 549.
[55] J. Zhao, A. Swinnen, G. Van Assche, J. Manca, D. Vanderzande, B. V. Mele, *J. Phys. Chem. B* **2009**, *113*, 1587.
[56] B. C. Schroeder, Y.-C. Chiu, X. Gu, Y. Zhou, J. Xu, J. Lopez, C. Lu, M. F. Toney, Z. Bao, *Adv. Electron. Mater.* **2016**, n.
[57] E. Verploegen, R. Mondal, C. J. Bettinger, S. Sok, M. F. Toney, Z. Bao, *Adv. Funct. Mater.* **2010**, *20*, 3519.
[58] P. E. Hopkinson, P. A. Staniec, A. J. Pearson, A. D. F. Dunbar, T. Wang, A. J. Ryan, R. A. L. Jones, D. G. Lidzey, A. M. Donald, *Macromolecules* **2011**, *44*, 2908.
[59] A. J. Pearson, T. Wang, R. A. L. Jones, D. G. Lidzey, P. A. Staniec, P. E. Hopkinson, A. M. Donald, *Macromolecules* **2012**, *45*, 1499.
[60] N. D. Treat, C. G. Shuttle, M. F. Toney, C. J. Hawker, M. L. Chabinyc, *J. Mater. Chem.* **2011**, *21*, 15224.
[61] B. A. Collins, J. R. Tumbleston, H. Ade, *J. Phys. Chem. Lett.* **2011**, *2*, 3135.
[62] N. D. Treat, M. A. Brady, G. Smith, M. F. Toney, E. J. Kramer, C. J. Hawker, M. L. Chabinyc, *Adv. Energy Mater.* **2010**, *1*, 82.
[63] P. Kohn, Z. Rong, K. H. Scherer, A. Sepe, M. Sommer, P. Müller-Buschbaum, R. H. Friend, U. Steiner, S. Hüttner, *Macromolecules* **2013**, *46*, 4002.
[64] W. Yin, M. Dadmun, *ACS Nano* **2011**, *5*, 4756.
[65] R. J. Kline, M. D. McGehee, E. N. Kadnikova, J. Liu, J. M. J. Fréchet, *Adv. Mater.* **2003**, *15*, 1519.
[66] F. Liu, M. A. Brady, C. Wang, *European Polymer Journal* **2016**.
[67] S. Swaraj, C. Wang, H. Yan, B. Watts, J. Lüning, C. R. McNeill, H. Ade, *Nano Lett.*

**2010**, *10*, 2863.
[68] B. A. Collins, J. E. Cochran, H. Yan, E. Gann, C. Hub, R. Fink, C. Wang, T. Schuettfort, C. R. McNeill, M. L. Chabinyc, H. Ade, *Nat Mater* **2012**, *11*, 536.
[69] J. J. van Franeker, M. Turbiez, W. Li, M. M. Wienk, R. A. J. Janssen, *Nat Commun* **2015**, *6 SP* -, 1.
[70] A. L. Patterson, *Phys. Rev.* **1939**, *56*, 978.
[71] P. Cheng, X. Zhan, *Chem. Soc. Rev.* **2016**, *45*, 2544.
[72] S. Bertho, G. Janssen, T. J. Cleij, B. Conings, W. Moons, A. Gadisa, J. D'Haen, E. Goovaerts, L. Lutsen, J. Manca, D. Vanderzande, *Solar Energy Materials and Solar Cells* **2008**, *92*, 753.
[73] T. G. Fox, P. J. Flory, *J. Appl. Phys.* **1950**, *21*, 581.
[74] D. Leman, M. A. Kelly, S. Ness, S. Engmann, A. Herzing, C. Snyder, H. W. Ro, R. J. Kline, D. M. DeLongchamp, L. J. Richter, *Macromolecules* **2015**, *48*, 383.
[75] J. A. Emerson, D. T. W. Toolan, J. R. Howse, E. M. Furst, I. Thomas H Epps, *Macromolecules* **2013**, *46*, 6533.
[76] T. M. Burke, S. Sweetnam, K. Vandewal, M. D. McGehee, *Adv. Energy Mater.* **2015**, *5*, n.
[77] F. C. Jamieson, E. B. Domingo, T. McCarthy Ward, M. Heeney, N. Stingelin, J. R. Durrant, *Chem. Sci.* **2012**, *3*, 485.
[78] T. Earmme, Y.-J. Hwang, N. M. Murari, S. Subramaniyan, S. A. Jenekhe, *J. Am. Chem. Soc.* **2013**, *135*, 14960.
[79] E. Gann, A. T. Young, B. A. Collins, H. Yan, J. Nasiatka, H. A. Padmore, H. Ade, A. Hexemer, C. Wang, *Rev. Sci. Instrum.* **2012**, *83*, 045110.
[80] J. Ilavsky, *Journal of Applied Crystallography* **2012**, *45*, 324.

**Comparison of the morphology development of polymer-fullerene and polymer-polymer solar cells during solution blade coating**

*Xiaodan Gu, Hongping Yan, Tadanori Kurosawa, Bob C. Schroeder, Kevin L. Gu, Yan Zhou, John W. F. To, Stefan D. Oosterhout, Victoria Savikhin, Francisco Molina-Lopez, Christopher J. Tassone, Stefan C.B. Mannsfeld, Cheng Wang, Michael F. Toney*[*], *Zhenan Bao*[*]

ToC figure